Convectively Generated Potential Vorticity in Rainbands and Formation of the Secondary Eyewall in Hurricane Rita of 2005

FALKO JUDT AND SHUYI S. CHEN

Rosenstiel School of Marine and Atmospheric Science, University of Miami, Miami, Florida

ABSTRACT

Eyewall replacements in mature tropical cyclones usually cause intensity fluctuations. One reason for eyewall replacements remaining a forecasting challenge is the lack of understanding of how secondary eyewalls form. This study uses high-resolution, full-physics-model forecast fields of Hurricanes Katrina and Rita (2005) to better understand potential vorticity (PV) generation in the rainbands and the role that convectively generated PV played in the formation of a secondary eyewall in Hurricane Rita. Previous studies have focused on dynamic processes in the inner core and/or the effects of certain specified PV distributions. However, the initial development of a concentric PV ring in the rainband region has not been fully addressed. Katrina and Rita were extensively observed by three research aircraft during the Hurricane Rainband and Intensity Change Experiment (RAINEX), which was designed to study the interaction of the rainbands and the inner core. Rita developed a secondary eyewall and went through an eyewall replacement cycle, whereas Katrina maintained a single primary eyewall during the RAINEX observation period before landfall. These distinct features observed in RAINEX provide a unique opportunity to examine the physical and dynamical processes that lead to formation of concentric eyewalls. A triply nested high-resolution model with 1.67-km resolution in the innermost domain, initialized with operational model forecasts in real time during RAINEX, is used in this study. Analyses of wind, vorticity, PV, and vortex Rossby wave (VRW) activity in the inner-core region were conducted using both RAINEX airborne observations and model output. The results show that a higher PV generation rate and accumulation in the rainband region in Rita leads to a secondary PV/vorticity maximum, which eventually became the secondary eyewall. A strong moat area developed between the primary eyewall and the concentric ring of convection in Rita, prohibiting VRW activity. In contrast, VRWs propagated radially outward from the inner core to the rainband region in Katrina. The VRWs were not a contributing factor in the initial formation of the secondary eyewall in Rita since the moat region with near-zero PV gradient did not allow for radial propagation of VRWs. The large accumulation of convectively generated PV in the rainband region was the key factor in the formation of the secondary eyewall in Rita.

1. Introduction

Intensity changes of mature tropical cyclones (TCs) are controlled by both environmental conditions and internal structure changes. The environmental conditions such as vertical wind shear, moisture distribution, and the upper ocean temperature determine the maximum intensity a TC can reach under given conditions. Structure changes in a TC's inner core can lead to intensity changes even if the environmental factors remain unaltered. Although formation of a secondary eyewall in a TC and its impact on the TC's intensity is usually viewed in the context of the latter category, the interaction between a TC and its environmental conditions could be an important factor. The formation of a secondary eyewall can lead to weakening and/or decay of the primary eyewall in a TC. After the primary eyewall collapses, the secondary or outer eyewall assumes its predecessor's role and frequently contracts, leading to reintensification of the cyclone. This process, referred to as the eyewall replacement cycle (EWRC), can occur multiple times during a TC's life cycle (Willoughby et al. 1982). Although concentric eyewalls and ERWCs are observed in some intense TCs (Black and Willoughby 1992; Oda et al. 2005; Houze et al. 2006, 2007), not all major TCs develop these features. In this study, we will address why some intense TCs develop secondary eyewalls and others do not.

Corresponding author address: Dr. Shuyi S. Chen, Rosenstiel School of Marine and Atmospheric Science, University of Miami, 4600 Rickenbacker Causeway, Miami, FL 33149.
E-mail: schen@rsmas.miami.edu

Theoretical and modeling studies have most focused on dynamic processes in the inner core of TCs to explain EWRCs. Vortex Rossby wave (VRW) theory plays a major role in our current understanding of these inner-core dynamics (Guinn and Schubert 1993; Montgomery and Kallenbach 1997, hereafter MK97; Chen and Yau 2001; Wang 2002a,b). One of the hypotheses in MK97 was that VRWs can accelerate the mean tangential flow at some distance from the storm center through eddy momentum flux convergence. This process could generate a secondary wind maximum, a necessary condition characterizing the secondary eyewall (Samsury and Zipser 1995). Other studies used certain specified vorticity or potential vorticity (PV) structures to simulate secondary vorticity maxima that were observed in TCs undergoing EWRCs. Kossin et al. (2000) used concentric vorticity rings in their idealized model to study the interactions between the primary and secondary eyewalls. Kuo et al. (2004, 2008) applied a highly simplified, nondivergent, and barotropic vorticity model to investigate interactions between two patches of vorticity. However, the simplicity and highly idealized assumptions in these studies pose the question of whether the results are truly applicable to real TCs. Furthermore, an important question remaining is how the specified PV distributions, such as concentric rings, arise in real TCs.

Several studies have used high-resolution, full-physics models with idealized initial and lateral boundary conditions to study secondary eyewalls (Chen and Yau 2001; Wang 2002a,b; Terwey and Montgomery 2008). It is unclear whether there were secondary eyewalls and/ or EWRCs in some of these studies since the secondary wind maximum was not shown, such as in Terwey and Montgomery (2008). They used a secondary vertical velocity maximum as a proxy, which may be correlated with convection but is not necessarily representative of a true secondary eyewall with a secondary wind maximum. Another peculiar feature shown in Terwey and Montgomery (2008) is that the simulated storm went through a rapid intensification during an EWRC, which is inconsistent with all existing observations. Others have attributed EWRCs to factors that are intrinsic to a TC's inner core such as VRWs. However, the question of why some TCs undergo EWRCs and others do not has not been addressed. Given the observation that only 30% of Atlantic Ocean hurricanes develop secondary eyewalls during their lifetime (Kossin and Sitkowski 2009), it seems questionable that TC inner-core processes alone can explain secondary eyewall formation.

Observational studies have shown that a horizontal jet related to intense outer rainbands seems to play a role in the formation of a secondary eyewall (Barnes et al. 1983; Hence and Houze 2008, hereafter HH08). In 2005, the Hurricane Rainband and Intensity Change Experiment (RAINEX) deployed three research aircraft with airborne Doppler radars to observe hurricane rainbands and the inner-core regions simultaneously to better understand the formation of secondary eyewalls and their interaction with the primary eyewall. RAINEX collected comprehensive airborne data in Hurricanes Katrina and Rita. During the multiday observation periods in each of these category-5 hurricanes, Rita developed a secondary eyewall that eventually replaced the primary eyewall. Katrina, in contrast, maintained a single primary eyewall until the storm made landfall. Although Blackwell et al. (2008) speculated that an eyewall replacement cycle occurred in Katrina before landfall, there is no observation showing a consistent secondary wind maximum surrounding the storm as observed in Rita, except on the east side of the storm center where the wind field broadened significantly on 29 August, with a wind maximum at larger radii (M. Black 2008, personal communication).

These distinct differences in Rita and Katrina provided a unique opportunity to examine the physical and dynamical processes affecting the formation of concentric eyewalls. This study investigates the differences in PV generation by convection in the rainband regions of Hurricanes Rita and Katrina. These differences play a key role in the formation of Rita's secondary eyewall. High-resolution, cloud-resolving model forecast fields obtained in real time during RAINEX are used to explain the physical and dynamic processes. The model results are compared with the RAINEX observations to evaluate and validate the evolution in hurricane structure in both storms.

2. Model and data

a. The numerical model

The numerical model used in this study is the nonhydrostatic fifth-generation Penn State University–National Center for Atmospheric Research Mesoscale Model (MM5; Grell et al. 1994; Dudhia 1993). To capture the long life cycle of hurricanes and to resolve the inner-core structure, Tenerelli and Chen (2001) developed a vortex-following nested grid that allows the model to be integrated for five days or longer at high resolution (~1–2 km) in the innermost domains. During the RAINEX field program, a triply nested model system with 15-, 5-, and 1.67-km grid spacing, respectively, was used for real-time forecasts and aircraft mission planning. The two inner domains move automatically with the storm. The domain sizes for each of the inner nests are 121 × 121 and 151 × 151, respectively. There are 28 sigma levels in the vertical with about nine levels

within the atmospheric boundary layer. The model was used to simulate Hurricane Bonnie (1998) (Rogers et al. 2003), Hurricane Georges (1998) (Cangialosi et al. 2006), and Hurricanes Floyd (1999) and Frances (2004) (Chen et al. 2007). These studies showed that it is necessary to use a 1.67-km grid spacing to properly simulate the hurricane evolution and intensity change.

A modified Kain–Fritsch cumulus parameterization scheme is used on the 15-km grid (Kain and Fritsch 1993). Modifications to the Kain–Fritsch parameterization include detrainment of 30% of the hydrometeors to the resolvable grids and a higher vertical velocity threshold for initiation of convective clouds, which is more suitable for tropical oceanic conditions. The inner core of the hurricanes is simulated explicitly in cloud-resolving mode. The microphysics scheme used on all three grids is based on Tao et al. (1993). The Blackadar PBL scheme (Zhang and Anthes 1982), also used on all grids, was modified over water. We introduced different roughness parameters for temperature z_t and moisture z_q, which are different from z_0 for momentum based on Garratt (1992).

During the RAINEX field program, high-resolution MM5 forecasts were made with various large-scale operational model forecasts as initial and lateral boundary conditions, including Geophysical Fluid Dynamics Laboratory (GFDL), Global Forecast System, Canadian Meteorological Centre, and Navy Operational Global Atmospheric Prediction System (NOGAPS) models. To understand the physical and dynamical processes in the evolution of storm structures, two MM5 forecasts with the model forecast tracks closest to the National Hurricane Center (NHC) best-track data are selected for this study: 1) the 3-day model forecast initialized at 0000 UTC 27 August 2005 with the GFDL model forecast fields as the lateral boundary condition and 2) the 5-day forecast initialized at 0000 UTC 20 September 2005 with the NOGAPS forecast fields as the lateral boundary condition. A vortex relocation method was used in both cases to start the simulations with more realistic vortices. The MM5 output was transformed onto a cylindrical grid in a storm-relative framework in which the storm center was defined by a center-finding algorithm using geopotential height fields at each level (Tenerelli and Chen 2001). Then the Cartesian grid output was interpolated to the cylindrical grid with 1° spacing in the azimuthal direction and 2-km spacing in the radial direction. This process made it easier to decompose atmospheric fields into wavenumber space and calculate azimuthal mean and perturbation components. To capture the finescale, high-frequency features the model forecasts were rerun for part of the time period with 12-min output intervals.

The lower boundary condition over the ocean for the uncoupled MM5 is from a product using both microwave satellite SST and the National Centers for Environmental Prediction SST analysis fields (Chen et al. 2001). The SST remains unchanged during the model forecast periods for both storms.

b. Aircraft observations from the RAINEX field program

Hurricanes Katrina and Rita were sampled frequently during the RAINEX field program. The airborne observations in these storms allow for investigation of the evolution in more detail than otherwise would have been possible. In addition to flight level and dropsonde data, the Doppler radars on board the two National Oceanic and Atmospheric Administration (NOAA) WP-3D and one Naval Research Laboratory (NRL) P-3 aircraft provided both radar reflectivity and three-dimensional wind fields. We also calculated the vertical vorticity component from the 3D Doppler wind fields. The NRL P-3 was equipped with the Electra Doppler Radar (ELDORA), which provided very high resolution observations (400–800 m). This resolution made it possible to analyze small-scale features such as convective updrafts and downdrafts and convective-scale wind and vorticity perturbations.

3. Hurricanes Katrina and Rita

a. Track and intensity

Katrina and Rita were two category-5 hurricanes in the Gulf of Mexico during the record hurricane season in 2005. The MM5 forecast tracks are relatively close to the observed ones in terms of landfall locations in both cases (Fig. 1). However, the forecasts are about 12–18 h too fast over the 5-day period for Rita and about 6 h for Katrina when compared with the best-track data (Fig. 1). Both storms underwent rapid intensification in the Gulf of Mexico, which was captured by the model forecasts (Fig. 2). Rita developed a secondary eyewall on 21–22 September and went through a subsequent EWRC on 23 September (Houze et al. 2007). It experienced an increase in vertical wind shear later on 23 September (e.g., Houze et al. 2006) and weakened about 40 h prior to making landfall near the Texas coast on 24 September 2005 (Fig. 2a). RAINEX observations showed that the initial weakening on 22 September was due to the development of the secondary eyewall and EWRC (Houze et al. 2007). The model predicted this event and many observed features, although the timing was about 8–12 h earlier than observed (Fig. 2a). Because of the early timing, the model-forecast Rita reintensified after the
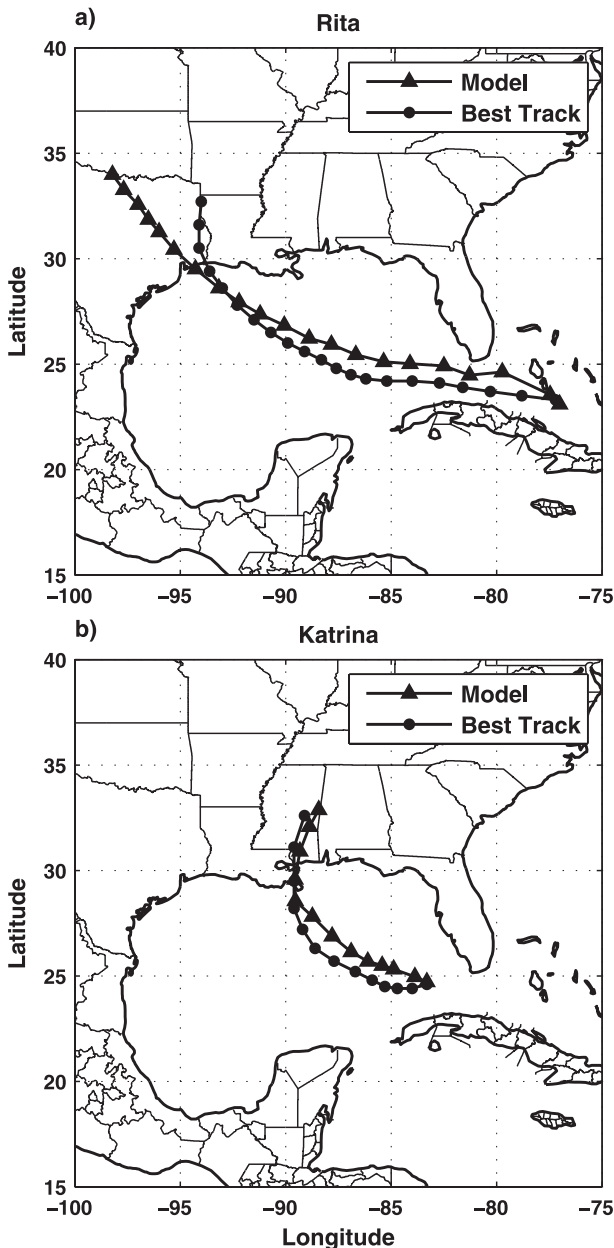
FIG. 1. Storm tracks from MM5 and the NHC best-track data for (a) Hurricane Rita, 0000 UTC 20–25 Sep 2005, and (b) Hurricane Katrina, 0000 UTC 27–30 Aug 2005.
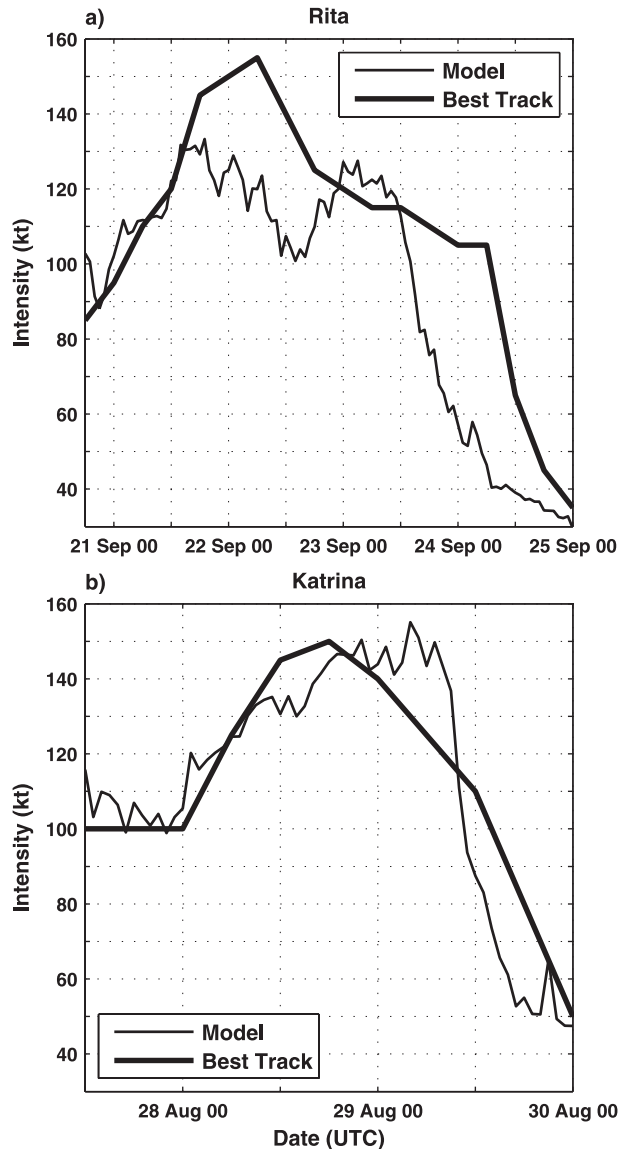

FIG. 2. Maximum surface wind speeds from MM5 (thin line) and the NHC best-track data (thick line) for (a) Hurricane Rita, 0000 UTC 20–25 Sep 2005, and (b) Hurricane Katrina, 0000 UTC 27–30 Aug 2005.

EWRC as the new primary eyewall contracted before running into the enhanced vertical wind shear, whereas the observed storm did not reintensify because of the shear.

In the case of Katrina, the model forecast did not weaken on 29 August before making landfall near New Orleans as observed (Fig. 2b). It could be related to the evolution of the model-forecast storm structure discussed in the following section and/or lack of coupling to the ocean. Ming et al. (2008) have shown that the model-simulated storm intensity in Katrina is weaker and closer to the observations when using a coupled atmosphere–ocean model in which the storm-induced mixing and upwelling in the ocean cools the near-surface temperature. It is difficult to pin down exactly the role of the upper ocean in this study using the uncoupled model results.

b. Storm structure

Evolution of a storm structure is a key to understand hurricane intensity change. Model-forecast rain, wind,
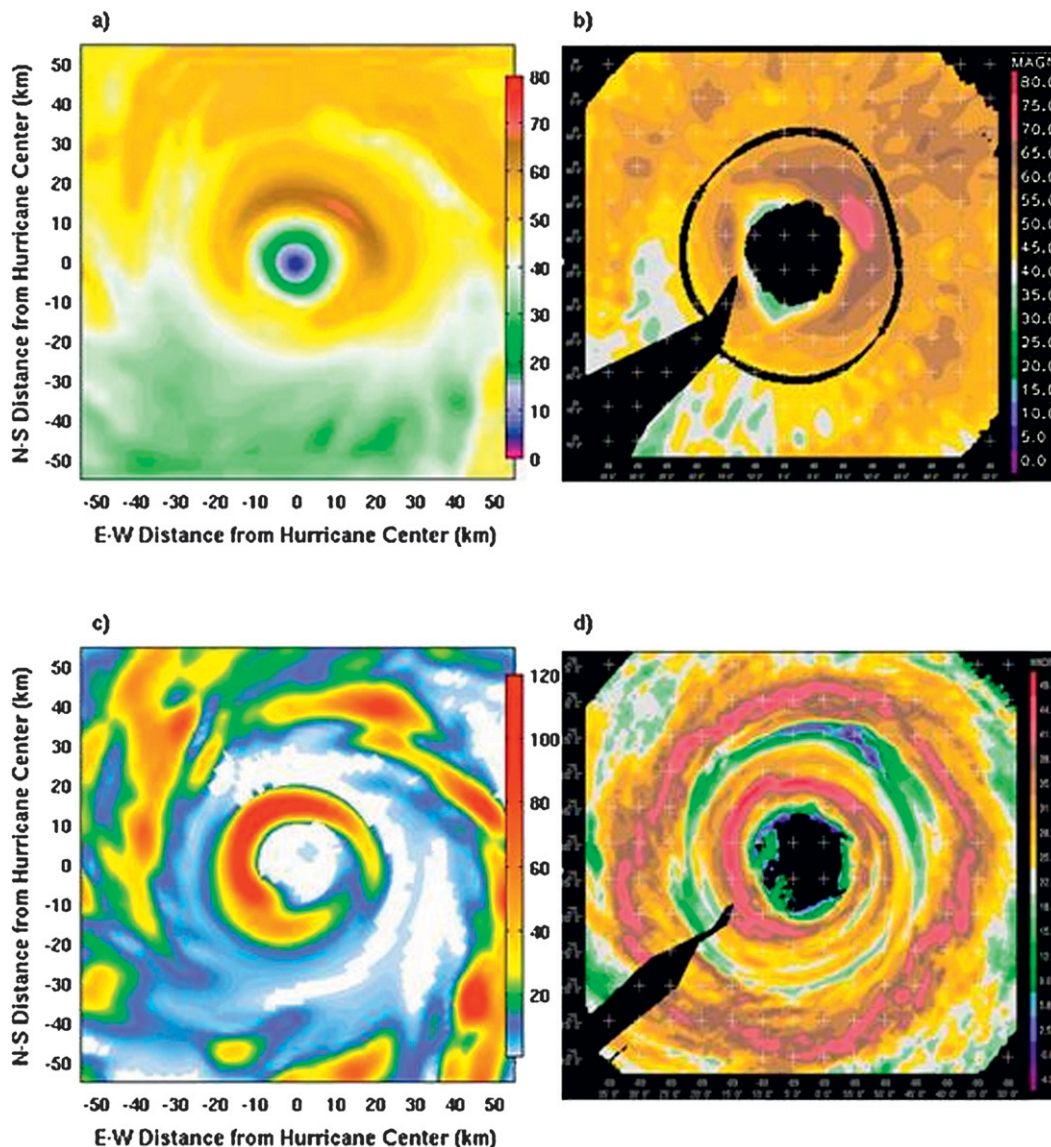
FIG. 3. MM5-forecast (a) wind speed (m s^{-1}) and (c) rain rate (mm h^{-1}) at the 700-hPa level at 0624 UTC 22 Sep, and ELDORA-observed (b) wind speed and (d) radar reflectivity (dBZ) composites at flight level ($\sim$2.5 km) between 1712 and 1742 UTC 22 Sep for Hurricane Rita. The horizontal scales in (b) and (d) are the same as in (a) and (c). [(b) and (d) Adapted from Bell et al. (2008).]

and vorticity fields are compared with the RAINEX observations to evaluate the results. Although the exact timing for model-forecast and observed EWRC is not the same because of uncertainties in the model initial conditions and model errors, the model output will be analyzed in a storm-relative sense in comparison with observations during the storm evolution. Figure 3 shows the inner-core structure of Rita's primary and secondary eyewalls on 22 September. Both the eyewall and secondary maxima in wind speed and precipitation were predicted quite well compared with observations from the ELDORA on board the NRL P3 aircraft (Bell et al.

2008). A key feature is the distinct moat region as described in Houze et al. (2007), that is, a minimum of precipitation and wind speed between the two concentric eyewalls. This is also evident in the model forecast fields (Figs. 3a,c). The ELDORA data show smaller-scale features than the model forecasts, partly because of the higher horizontal resolution of the radar ($\sim$400–800 m) than the model (1.67 km).

The evolution of Rita's concentric eyewalls was observed by multiple aircraft missions with Doppler radar over a course of three days (21–23 September) during RAINEX. Although it was not continuous in time, a

series of maps of vertical vorticity provided good coverage and a valuable dataset to compare with the model forecasts. The vertical vorticity is computed from the three-dimensional wind field retrieved from the airborne dual Doppler radar on board the NOAA P3 aircraft. The data from two flight legs across the storm center, usually in a figure-4 pattern over roughly 30–40 min for each leg, have been composited to obtain a vorticity distribution covering as much of the storm as possible. The retrieved vorticity field is then compared with the vertical vorticity from the model forecast at the same level (700 hPa) in a storm-evolution-relative time framework. The exact times of observed vorticity and model output do not match because the model-forecast storm underwent EWRC about 8–12 h earlier than the observed storm. Figure 4 shows the Doppler radar–derived and model-forecast vorticity fields at the 700-hPa level in Rita. In general, both the observation and model forecast show the commonly observed vorticity structure of a mature TC with the maximum values located inside of the radius of maximum wind (RMW) at ~20-km radius on 21 September (Figs. 4a,b). The missing data in the eye are due to the fact that there is no precipitation and therefore no return signal on the radar. There are elevated values of vorticity in the rainbands, especially outside of 50-km radius, which is likely generated by tilting and stretching of horizontal vorticity as proposed in HH08. The observed vorticity fields are relatively smooth, mainly because they are composites over a time period of 60–100 min, whereas the model output is an instantaneous "snapshot." Another factor is that the horizontal resolution of the Doppler radar data from the NOAA P3 aircraft is ~2–4 km, which is lower than the ELDORA data (~400–800 m) and the model innermost domain (1.67 km).

The vorticity in the rainband region increased significantly on the following day as observed from ~1500 to 1600 UTC 22 September (Fig. 4c) and similarly in the model forecast (Fig. 4d). The formation of a ringlike structure with a local maximum vorticity is evident at 50–60 km during the next a few hours (Figs. 4e,f). The secondary vorticity maximum became stronger and reached a value close to 4×10^{-3} s^{-1} as the secondary convective ring contracted inward by ~10 km in radius. The primary eyewall began to weaken as described in Houze et al. (2007). The storm continued the EWRC, although there was no research flight mission into Rita until the following day on 23 September. At that time, the secondary eyewall had replaced the original eyewall and become the new primary eyewall. The vorticity patterns in Figs. 4g and 4h are similar to that observed earlier on 21 September (Figs. 4a,b), except the new eyewall and eye are larger than the old ones. Rita

completed the EWRC but the storm intensity was weaker than prior to the EWRC on 21 September (Fig. 2a) because of the large eye and the new eyewall.

Unlike in Rita, there was only one NOAA P3 aircraft available during Katrina. Figure 5 shows the Doppler radar composites from flights on 28–29 August in comparison with corresponding model forecasts. The eye of Hurricane Katrina is smaller in the model forecast (Figs. 5b,d) compared with the observations (Figs. 5a,c) for both days, which explains the stronger storm intensity in the modeled storm (Fig. 2b). Although there is slightly enhanced vorticity in the rainband region on 28 August, it was much weaker than that in Rita. Katrina's rainbands displayed a typical spiral pattern on 29 August in both observation and model forecast, similar to that described in HH08. Another main difference between Katrina and Rita is the lack of a clear moat region in Katrina. There was no evidence of a secondary eyewall in Katrina on 29 August from the available observations during RAINEX.

c. Evolution of PV, wind, and rain

Although the RAINEX observations provided unprecedented data in terms of high-resolution radar coverage to describe the structural changes in Rita's inner-core and rainband regions during its EWRC, the lack of continued coverage in time makes it difficult to fully understand the development and evolution of the EWRC. The model output is used to examine the related physical and dynamical processes. To contrast the formation and evolution of the secondary eyewall and the EWRC in Rita with Katrina which did not develop a secondary eyewall, azimuthally averaged wind speed, rain rate, and PV are compared in time–radius diagrams shown in Fig. 6. The PV is displayed in a logarithmic scale since PV values in the eye region of a hurricane are an order of magnitude larger than outside the RMW. Figure 6e shows that elevated PV values in Rita's outer rainband region (75–125 km) can be traced back to 21 September and are related to an outer rainband (Fig. 6c). It is also evident that the secondary PV maximum becomes more pronounced with time while contracting radially inward. This secondary PV maximum precedes the development of the secondary wind maximum (Fig. 6a), which indicates the wind maximum is a result of the enhanced PV in the rainbands. Late on 22 September, the secondary PV maximum becomes stronger than the one of the inner eyewall while the EWRC is taking place. Figure 6 also shows a pronounced moat region between the rainbands and the primary eyewall from 25- to 75-km radii on 21–22 September, corresponding to a local PV minimum. It is unclear whether the moat is just a result of subsiding motion between the two eyewalls or if it plays
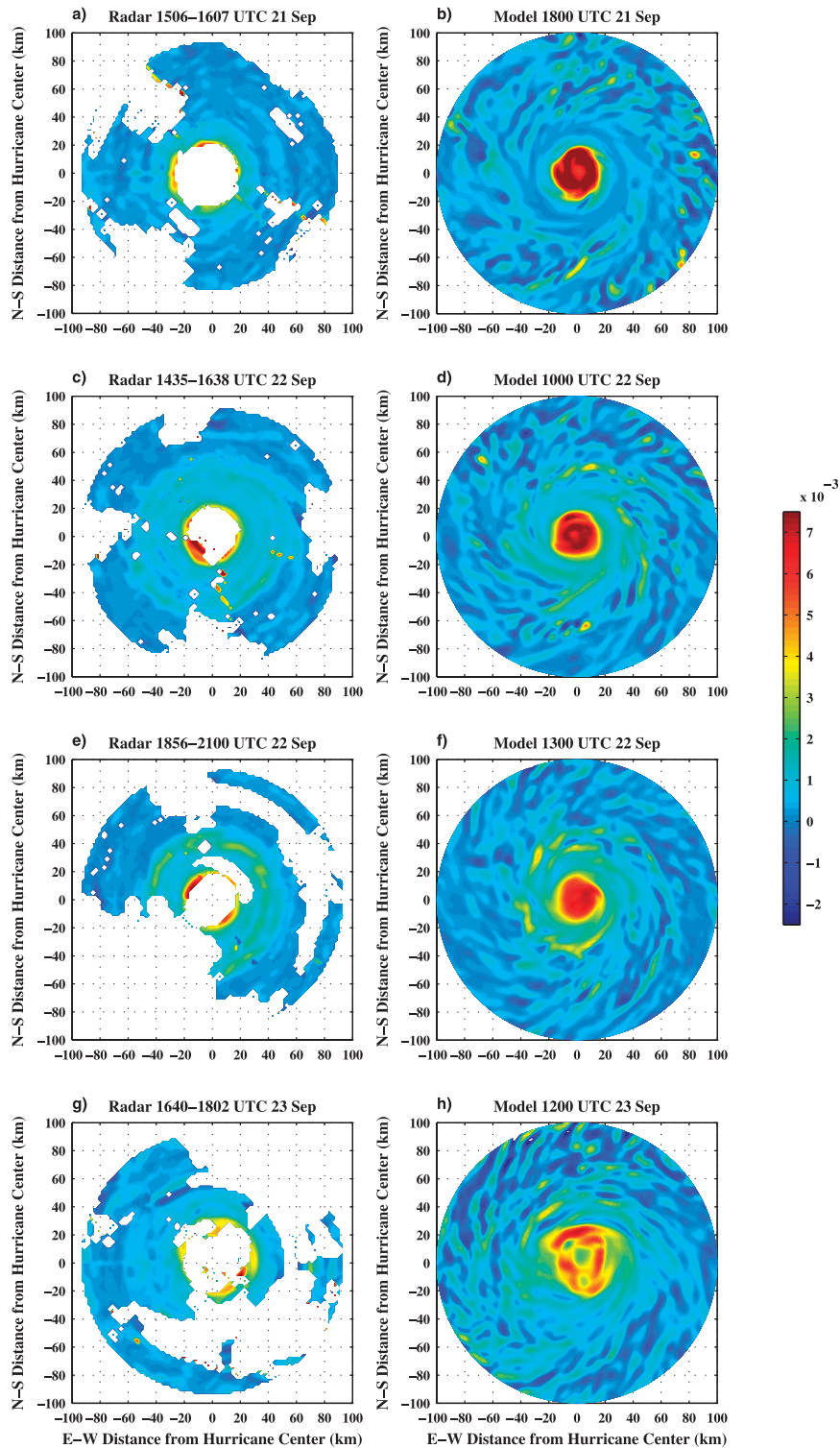
FIG. 4. (left) Vertical vorticity (s^{-1}) computed from the two NOAA P3 aircraft Doppler radar wind data at 3-km level and (right) model forecasts at 700 hPa from 21 to 23 Sep 2005 during Hurricane Rita. The aircraft data are composites within the time periods given on top of each panel on the left.
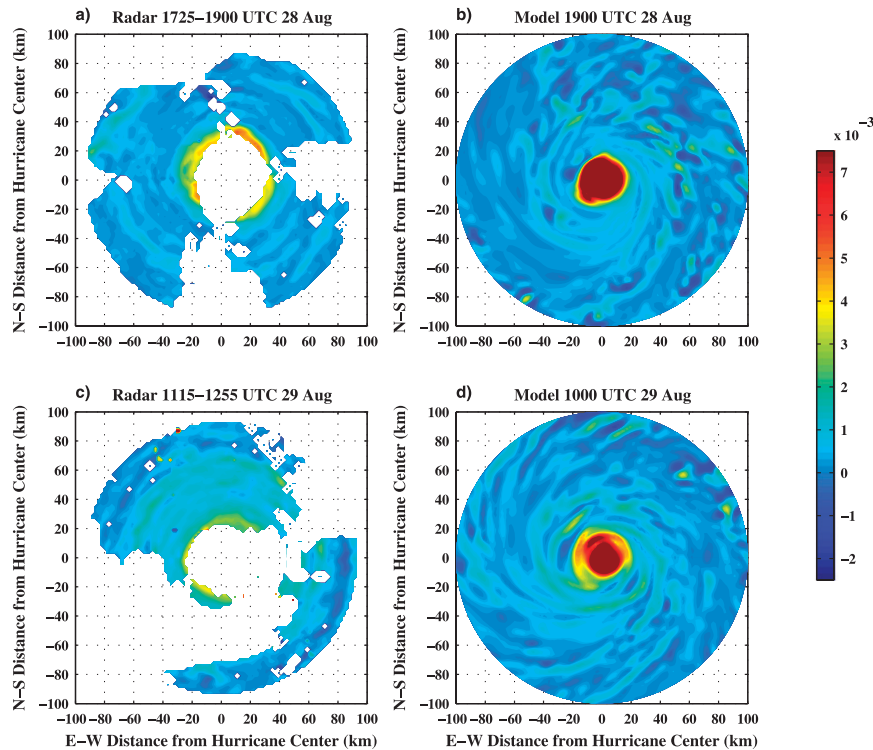
FIG. 5. As in Fig. 4, but for Hurricane Katrina from 28 to 29 Aug 2005.

an active role in the formation of a secondary eyewall (Houze et al. 2007).

The main difference in the evolution of the two storms is the outer rainband that led to a secondary PV and wind maximum in Rita but not in Katrina. The question is, What physical and dynamical processes are responsible for the development of the secondary PV maximum? By analyzing VRW activity as hypothesized in previous studies along with the PV generation characteristics in both storms, we hope to address this question quantitatively.

4. Vortex Rossby waves and their effect on storm evolution

Previous studies have indicated that VRWs may play a role in the formation of a secondary eyewall in TCs. Using an idealized dry model, MK97 proposed that eddy momentum fluxes could cause an increase in tangential winds at some distance from the storm center. To examine the role of VRWs in the model forecasts of Katrina and Rita, the model output was Fourier-decomposed into wavenumber-1–4 components. The results show that wavenumbers 1 and 2 are much more energetic than higher wavenumbers. Wang (2008) pointed out that higher-wavenumber asymmetries are axisymmetrized quickly by differential rotation of the vortex in the inner-core

region. The amplitudes of wavenumber-3 and -4 components are much smaller than those of the lower wavenumbers. Because the wavenumber-1 asymmetry in TCs is usually related to wind shear and/or cyclone motion (e.g., Chen et al. 2006), we focus on the wavenumber-2 component. To capture the high-frequency features, the model forecast fields had been output in 12-min intervals over a selected time period for both storms.

Figure 7 shows the wavenumber-2 component of rain-rate and PV fields. Both variables are highly correlated, indicating that rainbands in the inner-core region are reminiscent of VRWs as described in Chen and Yau (2001) and Wang (2002a,b). VRWs propagated outward from the eyewall to a radius of 60–80 km in Katrina (Fig. 7b). In contrast, there is no clear sign of outward propagation of VRWs from Rita's eyewall on 21 September (Fig. 7a), while rainbands and PV continue to strengthen in the outer rainband region. Furthermore, the moat region between the primary eyewall and the secondary ring of convection shows a distinct minimum of VRW activity. It may be unfavorable for convectively coupled waves because of subsidence-induced drying and increased static and inertial stability in the moat (Rozoff et al. 2006; Houze et al. 2007). Radially propagating VRWs in Rita developed later on 21–22 September. However, the waves did not originate in the inner eyewall as described in MK97 but rather formed in the
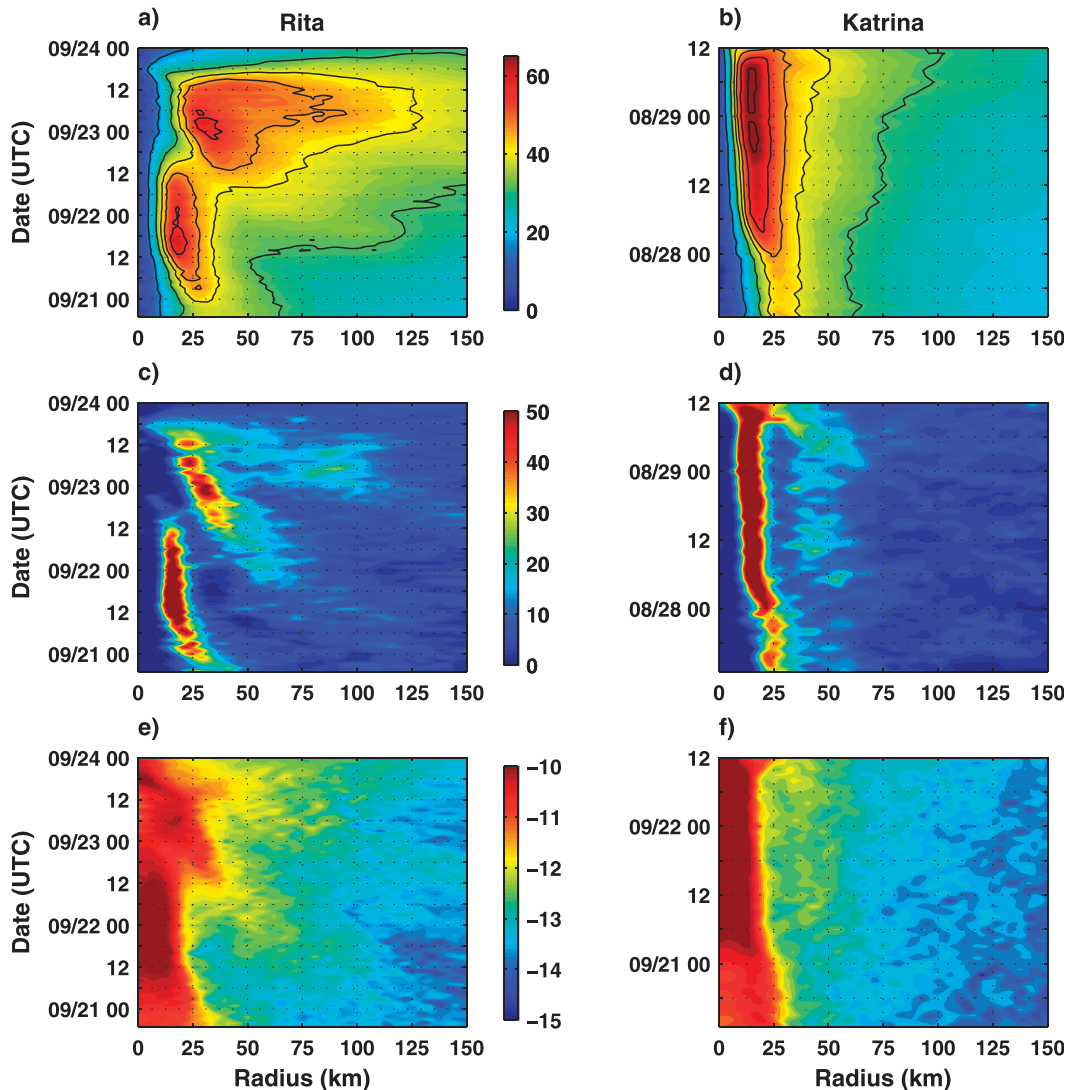
FIG. 6. Time–radius diagrams of azimuthally averaged (a),(b) wind speed at 700 hPa (m s^{-1}), (c),(d) rain rate (mm h^{-1}), and (e),(f) log(PV) at 700 hPa [PVU or 10^{-6} K m^2 kg^{-1} s^{-1}] from model forecasts for Hurricanes (left) Rita from 1800 UTC 20 Sep to 0000 UTC 24 Sep and (right) Katrina from 1200 UTC 27 Aug to 1200 UTC 29 Aug.

rainband region and propagated outward away from the storm center on the negative PV gradient associated with the convective ring. Once the secondary eyewall becomes the dominant eyewall, persistent radial propagating VRWs from the new eyewall were evident after 1200 UTC 22 September (Fig. 7a).

To examine further the rainband structures in relation to VRWs and the secondary eyewall formation, we computed the azimuthal fraction of convective precipitation at each given radius. The fractional coverage of intense convection is calculated as the number of grid points with a rain rate >12.5 mm h^{-1} and divided by the total number of grid points in the azimuthal direction in each radius. It shows the development of rainbands

concentrated in the outer region up to ~125-km radius in Rita in the early stage (Fig. 8a). The fractional coverage increases as the radius decreased with time, and the rainband eventually becomes the secondary eyewall with the fractional coverage close to 100%. As the ring of the intense outer rainband contracts in Rita, the moat becomes more pronounced and the primary eyewall weakens significantly. There is no evidence of radial propagating VRWs between the primary eyewall and the developing secondary eyewall (Fig. 8a). In contrast, the high fractional coverage outside of the primary eyewall in Katrina is due to the inner spiraling rainbands between 30- and 60-km radii (Fig. 8b). These rainbands are transient and correlate well with radially propagating VRWs.
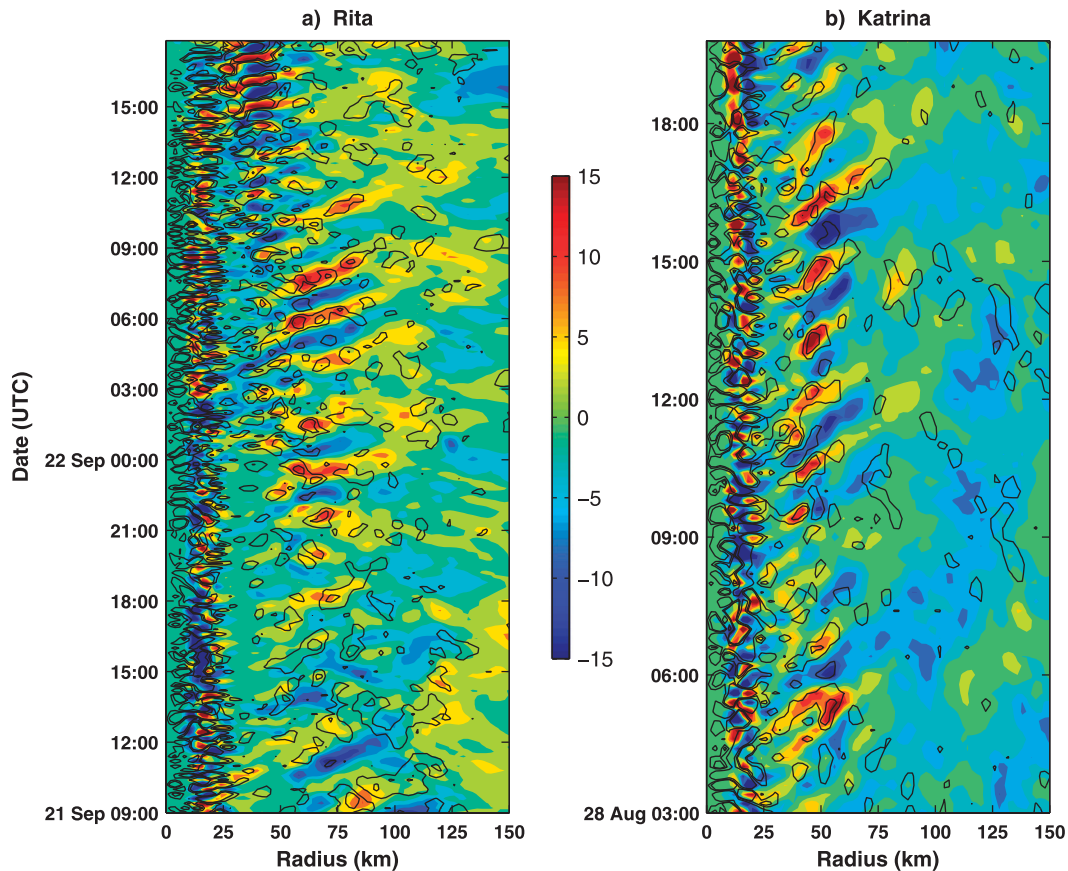
FIG. 7. Wavenumber-2 components of rain rate (color; mm h^{-1}) and PV (contours of 5 and 15 PVU) from model forecasts for Hurricanes (a) Rita from 0900 UTC 21 Sep to 1800 UTC 22 Sep and (b) Katrina from 0300 to 2000 UTC 28 Aug. The radial cross sections are taken from the storm center to the east at 700-hPa level.

An eddy momentum flux analysis can further provide a more quantitative assessment of how VRWs impact the dynamical structure of both storms. MK97 showed that outward-propagating VRW packets cease to travel at a particular radius, referred to as a "stagnation radius" at which wave–mean flow interactions can result in an increase of tangential wind speed. The acceleration of the tangential mean flow is determined by the eddy momentum flux divergence (EMFD) and can be expressed by the following equation:

$$\frac{\partial \overline{v}}{\partial t} = -\frac{1}{r^2}\frac{\partial}{\partial r}(r^2\,\overline{u'v'}), \qquad (1)$$

where r is the radius and v and u are the tangential and radial wind components. The overbar denotes the azimuthal mean, and primes are deviations from the mean. Figure 9 shows the azimuthally averaged EMFD over the 6-h periods between 0000 and 0600 UTC 22 September in Rita and between 0300 and 0900 UTC 28 August in Katrina, respectively. The tangential wind speed is given as a reference to show the location of the RMW. Eddies

convey momentum from the eyewall region (near the RMW; negative tendency) into the eye (positive tendency). Deceleration rates in the eyewall are greater than 11 m s^{-1} h^{-1}. The waves transport momentum into the eye, where the tangential wind speed is accelerated by 3 m s^{-1} h^{-1}. In contrast to MK97, however, this result does not support the hypothesis that VRWs deposit momentum at a certain radius (stagnation radius). The momentum tendency outside the inner core does not show a coherent structure and deviates little from the zero line. In Rita, the incoherent EMFD signal beyond 30 km is also found during the period in which the secondary eyewall was developing from 0000 to 0600 UTC 22 September—this process can be seen clearly in the azimuthally averaged wind speed (Fig. 9a). The EMFD outside the RMW is alternating in sign in a relatively nonperiodic manner, and there is no clear signal related to the secondary wind maximum at 60-km radius. The lack of a strong positive EMFD signal at radii outside the inner core indicates that this process did not play a major role in the storm-structure changes. From a momentum point of view, the wave–mean flow interactions
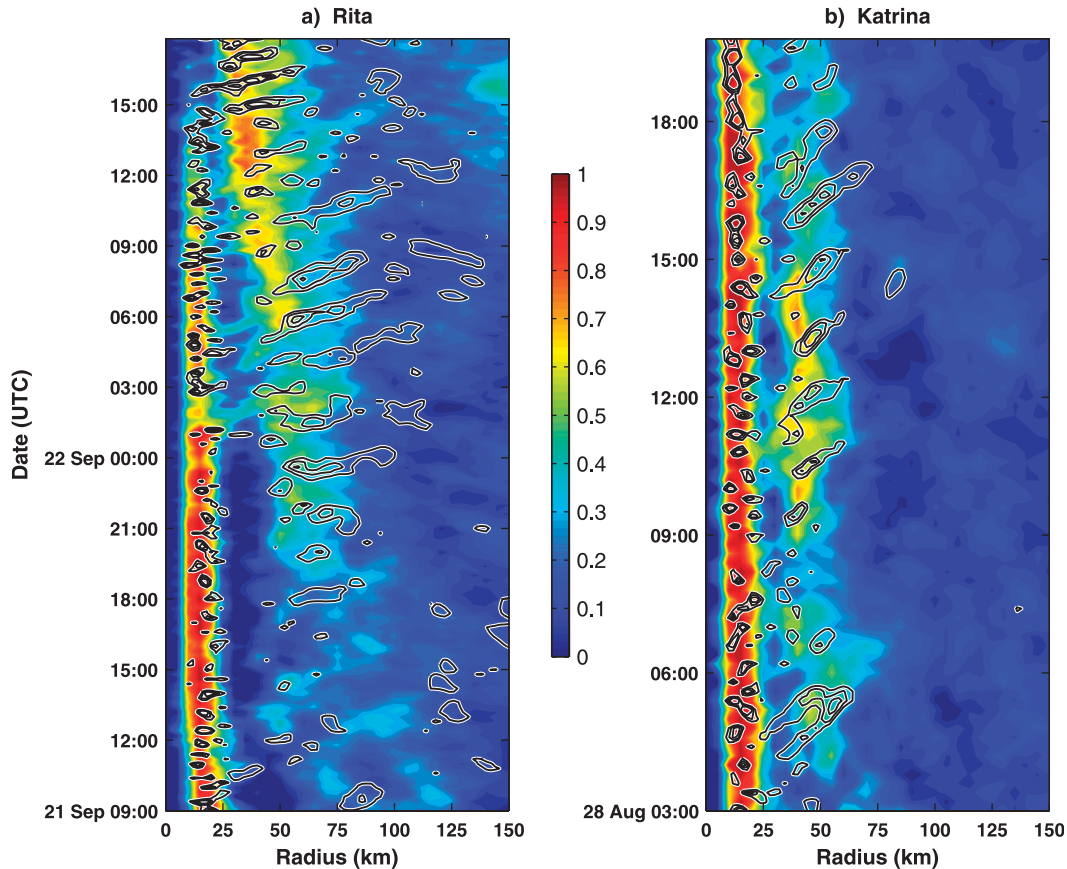
FIG. 8. Fractional coverage of rain rate >12.5 mm h^{-1} (color) and wavenumber-2 component of rain rate (contours of 5, 10, and 15 mm h^{-1}) from model forecasts for Hurricanes (a) Rita from 0900 UTC 21 Sep to 1800 UTC 22 Sep and (b) Katrina from 0300 to 2000 UTC 28 Aug.

are negligible for regions away from the immediate eyewall region. The VRW-induced momentum fluxes were not a contributor for the development of the secondary wind maximum in Rita.

5. Secondary eyewall formation in Rita

To address the key question of how the secondary PV and wind maxima developed in Rita, a PV budget analysis is conducted. Because the eddy momentum flux was not a source to accelerate the mean flow, the secondary wind maximum may be a dynamic response to the developing secondary PV maximum in the rainband region. Here we will focus on the role of convectively generated PV in Rita's secondary eyewall formation.

a. PV budget

The PV budget is computed similarly to that in Wang (2002a), except that the z coordinate is used as the vertical coordinate. HH08 have shown that PV is most efficiently generated in the rainbands where active

deep convection prevails. The best way to estimate the rate of PV generation is to decompose the PV budget equation into azimuthal mean and perturbation parts by making use of the Reynolds decomposition. The PV budget equation can be written as follows:

$$\frac{\partial \overline{P}}{\partial t} = -\nabla \cdot \left(\overline{\mathbf{v}} \overline{P} - \frac{\overline{Q}}{\rho} \overline{\boldsymbol{\omega}} + \overline{\mathbf{v}'P'} - \frac{1}{\rho} \overline{Q'\boldsymbol{\omega}'} \right). \quad (2)$$

The overbar denotes the azimuthal average of a variable and primes are the deviations from the azimuthal mean. The left-hand side of (2) is the local rate of change of azimuthally averaged PV (i.e., the PV tendency at a particular radius). The right-hand side of the equation is composed of the sink and source terms. The frictional dissipation term is considered to be negligible (Wang 2002a). The first right-hand-side term is the flux divergence of azimuthally averaged PV by the mean wind. In physical terms, this can be explained as the PV flux due to the mean vortex circulation. The second term denotes the contribution by the divergence of the product of azimuthally averaged diabatic heating $\overline{Q}$ and the
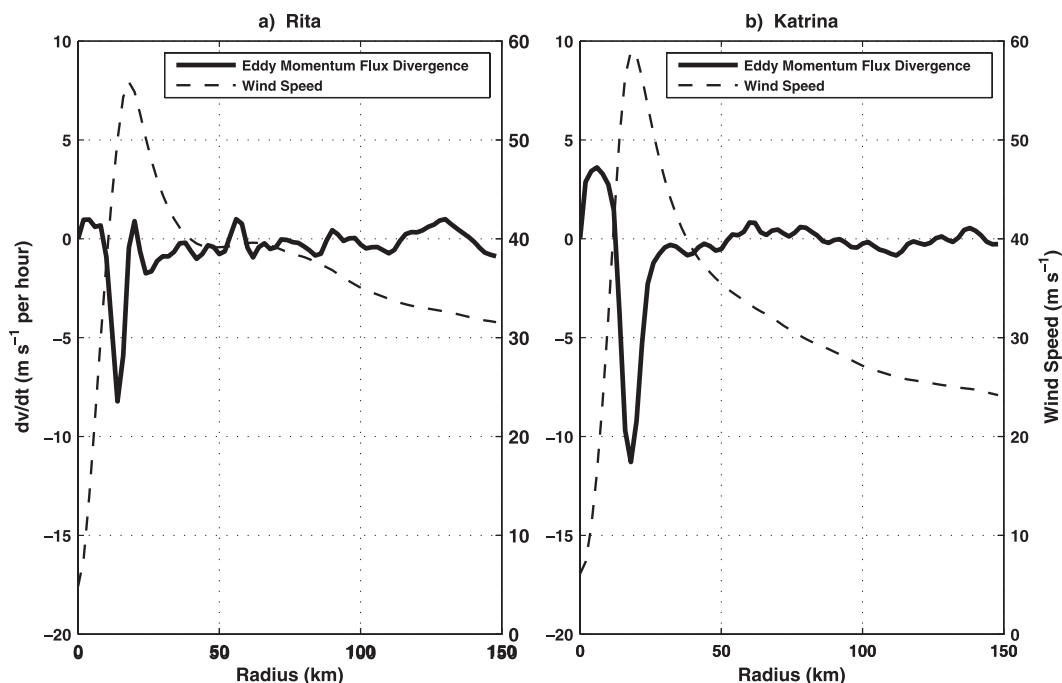
FIG. 9. Azimuthally averaged eddy momentum flux divergence (solid line) and tangential wind speed (dashed line) at 700 hPa from model forecasts for Hurricanes (a) Rita, time averaged between 0000 and 0600 UTC 22 Sep, and (b) Katrina, time averaged between 0300 and 0900 UTC 28 Aug.

averaged vorticity vector ($\overline{\boldsymbol{\omega}}$). The PV is generated when the heating gradient is positively aligned with the vorticity vector. This is usually the case in the eyewall and in rainbands below the level of maximum heating. The third term accounts for the flux divergence of asymmetric PV. The fourth term, of particular importance in this study, represents the PV generation by the perturbation diabatic heating and vorticity. Perturbations of the azimuthal mean heating and vorticity are manifestations of convective-scale elements. The contribution of heating and vorticity perturbations is again positive when the heating gradient perturbations coincide with positive vorticity vector maxima, which is the case in convective updrafts. Budget terms containing the wind vector **v** are only local sources or sinks; they redistribute PV and do not generate it in terms of the PV budget domain. The results of the PV budget analysis will be presented for two distinct regions: 1) the inner-core/ eyewall region and 2) the rainband region beyond ~40-km radius from the storm center.

b. The inner core

PV generation rates are greatest in the hurricane eyewalls. This is not surprising given that the vertical mass transport is largest in this region and both the heating gradient and vorticity vector are pointing in the same direction. Figure 10 shows the PV generation rates in Rita

and Katrina, averaged over a 6-h period. According to the PV budget equation in (2), two separate panels are shown for the contribution of the mean diabatic heating and vorticity term $[(\overline{Q}/\rho)\overline{\boldsymbol{\omega}}$; Fig. 10a] and the perturbation parts ($\rho^{-1}\overline{Q'\boldsymbol{\omega}'}$; Fig. 10b). The symmetry of the eyewall makes the contribution of the mean a dominant component. The PV generation rates approach 50 potential vorticity units (PVU) h^{-1} in Katrina's eyewall (Fig. 10a), where 1 PVU is defined as $10^{-6}\,\mathrm{K\,m^2\,kg^{-1}\,s^{-1}}$. These are the highest values found in this analysis. The azimuthally and temporally averaged rain rates and PV profiles are also shown to indicate the storm structure in terms of location and strength of the eyewall and rainbands. Katrina's PV generation rates in the inner core exceed Rita's since the storm is stronger and inner-core circulation is dominated by the strengthening eyewall. Inside the main PV generation region, between 10 and 15 km, a small area of PV depletion can be found in both storms (Fig. 10a). We speculate that this is due to diabatic cooling in downdrafts in the inner edge of the eyewall as proposed by Willoughby (1998). Figure 10b shows the PV generation by the perturbation components of the diabatic heating. The most striking feature is the PV sink region in the center of the eyewall, with positive values at the edges of the eyewall. Perturbations in the heating field are manifestations of convectively coupled VRWs. The waves redistribute PV from the main generation region in
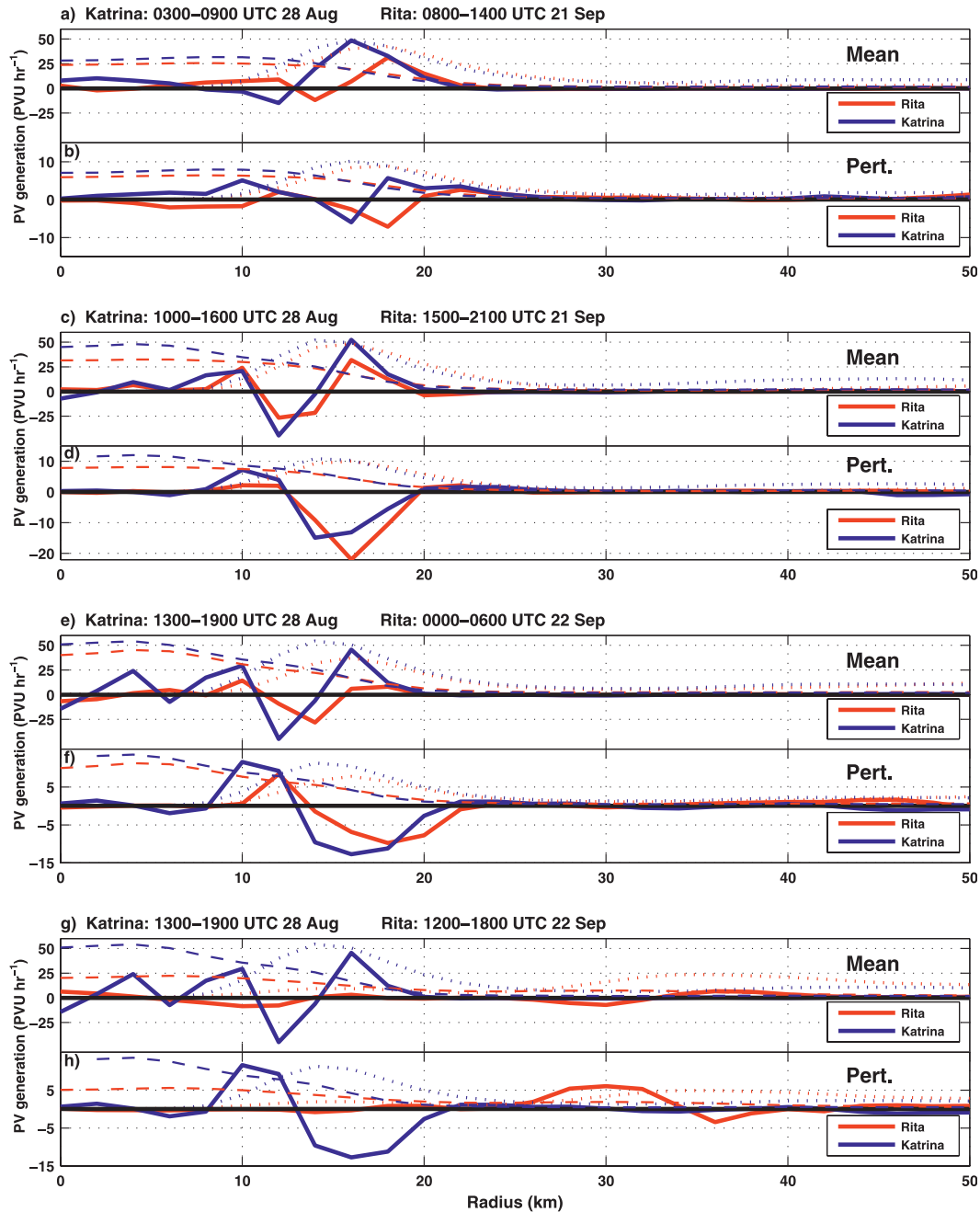
FIG. 10. PV generation rates (thick lines; PVU h^{-1}) due to (a),(c),(e),(g) the azimuthally averaged component ("Mean") and (b),(d),(f),(h) the perturbation component ("Pert.") in the PV budget equation, computed from the model forecasts for Hurricanes Rita and Katrina in the inner-core regions. Azimuthally averaged rain rates are shown with dotted lines, and PV is shown with dashed lines. Rita is in red, and Katrina is in blue. The 6-hourly time-averaging periods are indicated in each panel.

the eyewall downgradient into the eye away from the eyewall. They are part of the PV mixing dynamics described by Schubert et al. (1999).

In the subsequent 6-h period (Figs. 10c,d), the features are similar, indicating that the evolution of the two

storms is still comparable. Katrina has intensified faster than Rita, indicated by both higher PV generation rates of the azimuthally averaged diabatic heating and higher PV values in the eye (Fig. 10c). During the next 6-h period (Fig. 10e), Rita's primary eyewall weakens significantly.
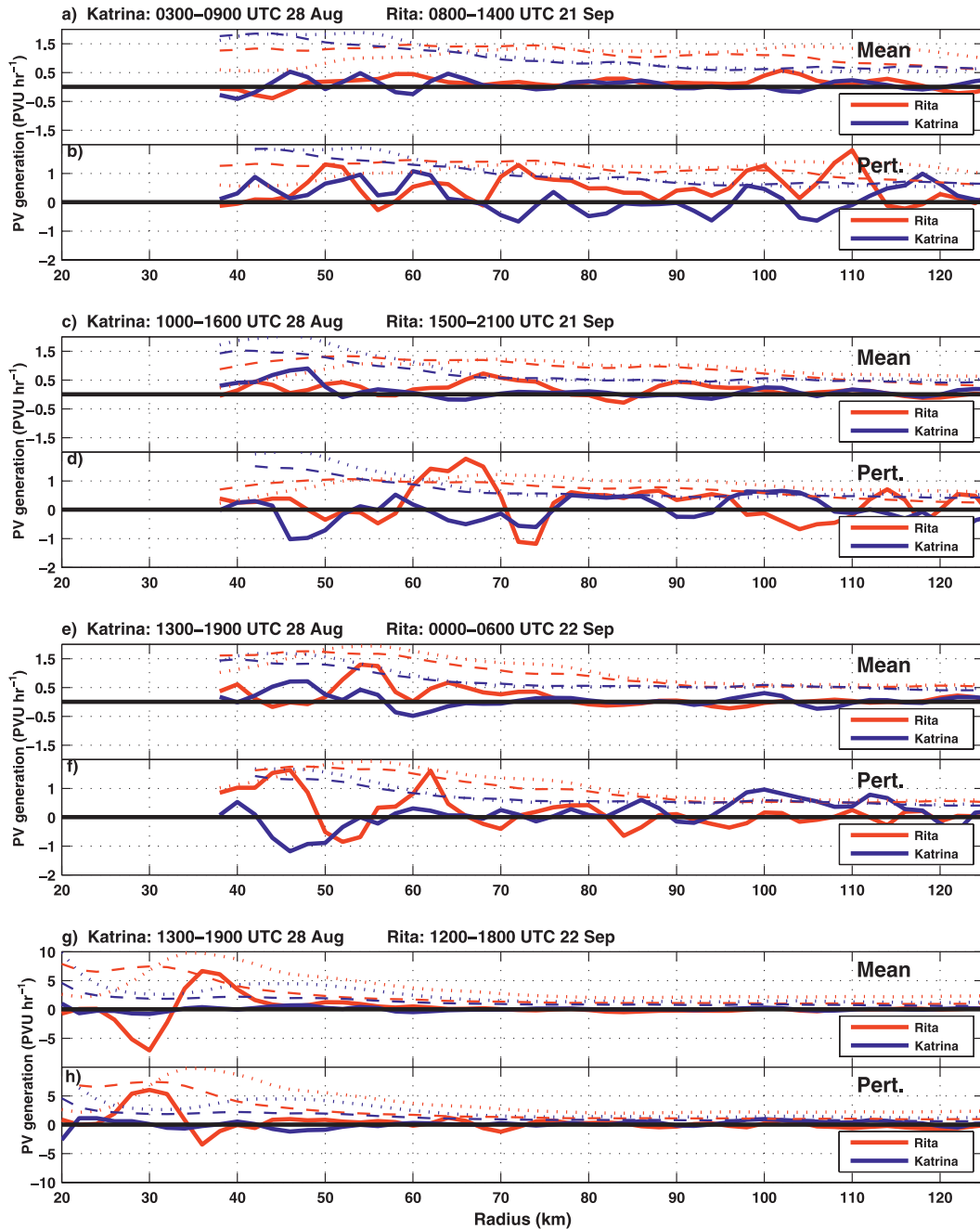
FIG. 11. As in Fig. 10, but for the rainband region.

The generation of PV by the mean heating has decreased and the amount of PV depleted is larger than the amount generated. The convection in the inner core weakens, which is associated with the ongoing EWRC in Rita. Note that the concentric ring in Rita becomes evident in the rain rate at 40–50-km radius. In the final 6-h period (Figs. 10g,h), there is little left of the original eyewall in Rita at the 15-km radius. The secondary eyewall becomes apparent in both the mean and

perturbation PV generation terms at ~35-km radius. The perturbation components now show a similar pattern to that of the original eyewall (Fig. 10b); the PV is being redistributed away from a region where generation rates by the mean component are positive.

c. Rainband regions

The PV generation rates in the rainband region between ~40- and 130-km radii are of particular importance.
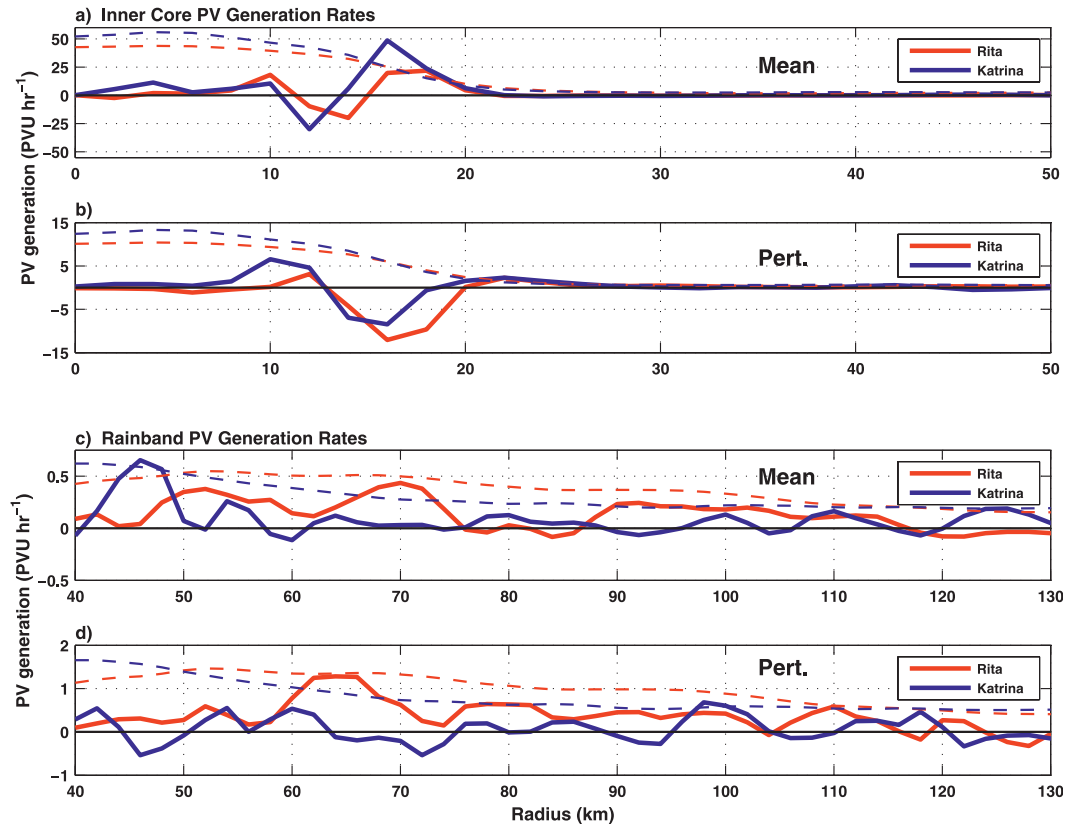
FIG. 12. (a),(b) As in Fig. 10 and (c),(d) as in Fig. 11, but averaged over the time periods 0800 UTC 21 Sep–1800 UTC 22 Sep for Rita and 0300–1900 UTC 28 Aug for Katrina.

It is in this region that the secondary PV ring forms and acquires eyewall characteristics. In general, absolute PV values and PV generation rates in regions farther away from the center are much smaller relative to the eyewall (because of this we used a logarithmic scale in Fig. 6), especially for the diabatic heating terms. This is due to the decreased fractional area covered by convection (Fig. 8) and the asymmetry of rainbands. In general, rainbands exhibit less of a circular pattern than the eyewall and contain large areas of stratiform precipitation. These regions are not conducive for intense pockets of PV generation over small areas.

A key result here is that the PV generation by the perturbation components is larger than the mean contributions at radii beyond 40 km from the center, which is reverse to that for the eyewall region. The 6-h averages of the mean and perturbation components are shown in Figs. 11a and 11b, respectively. Whereas Katrina's PV generation rates by the perturbations in the rainband region do not deviate much from zero between 60 and 120 km, Rita's PV generations are consistently larger and positive (Fig. 11b). The area of enhanced PV generation in Rita coincides with the rainbands, and the

temporally and azimuthally averaged PV profile continues to increase (Fig. 11). Although the PV generation rates may be small in comparison with the values in the eyewall (i.e., 1.5–2.0 PVU h^{-1} in the rainbands as compared with ~40 PVU h^{-1} in the eyewall in Rita), the rainband region covers a much larger area with positive PV tendencies. During the next 6-h period (Figs. 11c,d), Rita's elevated PV profile becomes more pronounced because of persistent PV generation, mainly by contributions from the perturbation term. By 22 September, the secondary PV maximum in Rita's rainband region acquires characteristics of an eyewall: the mean component (Fig. 11e) now shows a pronounced narrow peak at 55-km radius, whereas the contribution of the perturbation components is negative (Fig. 11f)—the concentric rainband has developed into an eyewall. Last, the secondary PV maximum in Rita resembles a mature eyewall similar to that seen in Fig. 11a. The perturbations are beginning to redistribute PV away from the new eyewall where the contribution by the mean is largest. This is opposite to the early stages of the secondary ring formation, where most PV was being generated by the perturbation components (Figs. 11b,d).

d. Secondary PV maximum and secondary eyewall formation

The comparison of the contributions of diabatic heating and vorticity perturbations in the rainband region reveals that the PV is being produced more effectively in Rita's rainband region. The persistence of the principal rainband in Rita, together with its optimal projection onto the azimuthal mean, seems to be a necessary condition for sufficient PV accumulation and the subsequent EWRC. Figure 12 summarizes what has been shown in Figs. 10 and 11 but for a longer time period, including the formation of the secondary eyewall in Rita. The generation rates in the inner core are qualitatively similar in both storms (Figs. 12a,b). However, Rita's PV generation rates in the rainband region are higher than in Katrina and are consistently above zero (Figs. 12c,d). The PV tendency in this area is positive over a long period, leading to the development of the secondary PV ring—the precursor of the secondary eyewall. To further emphasize the contrasting PV generation rates in the two hurricanes, the differences in PV generation rates (including both the mean and perturbation components) along with azimuthally averaged PV profiles in the two hurricanes are shown in Fig. 13. The difference is calculated by subtracting the generation rate in Katrina from that in Rita; positive PV generation rates thus show regions in which the PV generation rate in Rita is higher. The area between 60- and 120-km radii in Rita has significantly higher overall PV generation rates. This area correlates well with the secondary ring of PV that later becomes the secondary eyewall.

6. Conclusions

This study aims to understand better the dynamic processes of concentric eyewall formation and eyewall replacements in hurricanes. In particular, we address the effects of convectively generated PV in rainbands on the formation of secondary eyewalls. High-resolution MM5 forecasts of Hurricanes Katrina and Rita (2005) and observations from the RAINEX field program were used to investigate structural changes in the inner core and rainbands. The model forecasts captured the distinct evolutions of the two major hurricanes over the Gulf of Mexico, namely one with ERWC and one without, which was consistent with the RAINEX observations. These datasets provided a unique opportunity to examine the dynamic and physical processes involved in the EWRC. Detailed analyses of the evolving storm structures, PV distributions, PV tendencies, and comparison with observations have led to the following conclusions:
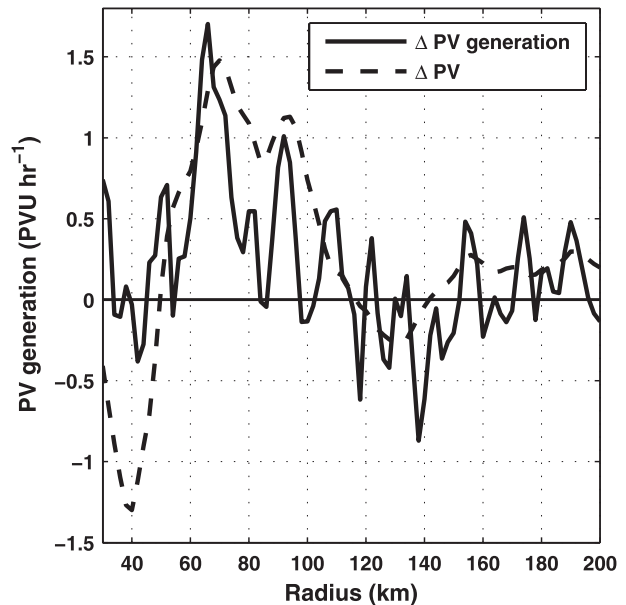

FIG. 13. Differences in azimuthally averaged PV (dotted line) and PV generation rate (solid line) between Hurricane Rita's and Katrina's rainband regions. The model forecasts are averaged from 0800 UTC 21 Sep to 1800 UTC 22 Sep for Rita and from 0300 to 1900 UTC 28 Aug for Katrina.

1) The model forecasts and observations both showed distinct rainband patterns in the two hurricanes. Rita's outer rainband was a clear manifestation of the principal band (Willoughby et al. 1982; Houze 2010). The outer band later consolidated into a secondary ring of convection with a moat region between the primary eyewall and the secondary ring. Convection in the concentric ring generated an enhanced ring of PV and wind velocity, which continued to intensify over time and finally became the new eyewall. Although Katrina had a similarly active principal band, the convection did not project as strongly onto the azimuthal mean. Furthermore, the storm developed active transient inner rainbands that were spiraling between the principal band and the primary eyewall. Unlike in Rita, there was no clear moat region in Katrina.

2) Vortex Rossby waves were active in both storms. However, they did not contribute to the formation of the secondary eyewall in Rita. The inner spiraling rainbands in Katrina were manifestations of VRWs. These rainbands were relatively short lived and therefore did not generate a clear secondary PV ring. More important, these rainbands were not associated with a secondary maximum in the azimuthally averaged wind speed and thus did not qualify as a secondary eyewall. In Rita, however, the analysis showed a different VRW pattern. During the formation stage of the secondary eyewall, the PV gradient was not conducive
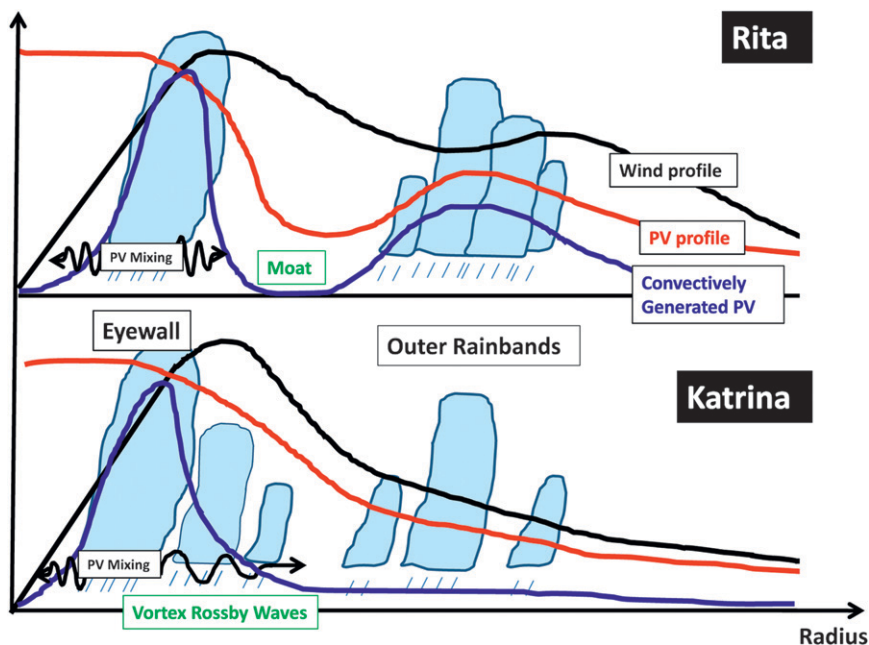
FIG. 14. Schematics of radial distributions of convection, vortex Rossby waves, azimuthally averaged tangential wind speed, PV, and PV generation by convection in Hurricanes Rita and Katrina. There are two distinct features: 1) significantly larger PV generation in the rainband region in Rita than in Katrina, which is a main contributing factor to the formation of the secondary eyewall in Rita, and 2) the absence of vortex Rossby wave propagation in the moat region between the primary and secondary eyewalls in Rita, which indicates that the waves are not a contributing factor.

for radial wave propagation and VRW activity was limited. Only after the secondary ring became more consolidated did the associated radial gradient support outward-propagating VRWs. Thus, we conclude that the secondary eyewall formed without interference from VRWs originating from the primary eyewall.

3) A detailed PV budget analysis showed that PV in the eyewall region is almost entirely generated through divergence of the product of mean heating and mean vorticity. In contrast, the majority of PV in the rainband region during the formation of the secondary eyewall is generated through eddy heating acting on eddy vorticity. Rita's PV generation rates in the outer rainband region were persistently larger at 60–120 km away from the center than those in Katrina and were responsible for the formation of the secondary eyewall in Rita. Figure 14 shows a schematic of distinct features and physical processes in the two storms, ultimately leading to their different evolutions. The inner-core PV generation patterns are similar in the two storms, with large PV generation rates in the eyewall. Eddies, including VRWs, convey PV from the main region of generation into the eye (mixing process) and radially away from the eyewall. In the outer region beyond the 80-km radius, however, the rates of PV generation by convection in Rita exceed the ones in Katrina by up to 100%. This is a manifestation of the principal rainband in Rita with convection projecting optimally onto the azimuthal mean. The shape of the rainbands plays an important role. The more circular the rainbands are, the better is the projection onto the azimuthal mean with more concentrated PV generation. Most of the PV is generated by distinct convective features since the perturbation components contribute more to the PV budget than the azimuthally averaged heating and vorticity term. In other words, the PV is mainly generated by convective updrafts and then projected onto the azimuthal mean because of the strong shearing stress in the circulation (axisymmetrization process). The convectively generated PV alters the wind field by generating a jet at and below the level of maximum heating, as observed by Barnes et al. (1983) and HH08. This process can enhance surface fluxes and thereby further strengthen convection in the outer rainbands. The rainbands then coalesce and eventually become a secondary eyewall.

The remaining question is why the rainbands in Katrina and Rita developed different patterns. If rainbands are

oriented in a more circular pattern around the storm center such as in the case of Rita, the convection in the rainbands concentrates PV generation at a particular radius, which increases the chances for a secondary eyewall to form. A hypothesis linking the pattern of rainbands to environmental conditions such as water vapor distribution will be tested in detail in a companion paper. The predictability of the formation of the secondary eyewall and EWRC may depend on whether the large-scale environmental conditions play an important role in the rainband patterns or the initial formation of the secondary PV maximum—as suggested by this study. If not—which would be the case if the initiation of an EWRC were determined by chaotic inner-core processes only—EWRCs might be inherently less predictable.

REFERENCES

Barnes, G. M., E. J. Zipser, D. Jorgensen, and F. Marks Jr., 1983: Mesoscale and convective structure of a hurricane rainband. *J. Atmos. Sci.,* **40,** 2125–2137.

Bell, M. M., W. C. Lee, R. A. Houze, B. Smull, and M. T. Montgomery, 2008: Axisymmetric concentric eyewall evolution in Hurricane Rita (2005). *Extended Abstracts, 28th Conf. on Hurricanes and Tropical Meteorology,* Orlando, FL, Amer. Meteor. Soc., 6C.1. [Available online at http://ams.confex.com/ams/28Hurricanes/techprogram/paper_137990.htm.]

Black, M. L., and H. E. Willoughby, 1992: The concentric eyewall cycle of Hurricane Gilbert. *Mon. Wea. Rev.,* **120,** 947–957.

Blackwell, K. G., A. Wimmers, C. Velden, P. J. Fitzpatrick, and B. Jelley, 2008: Hurricane Katrina's eyewall replacement cycle over the northern Gulf and accompanying double eyewalls at landfall: A key to the storm's huge size and devastating impact over a three-state coastal region. *Extended Abstracts, 28th Conf. on Hurricanes and Tropical Meteorology,* Orlando, FL, Amer. Meteor. Soc., 18C.6. [Available online at http://ams.confex.com/ams/28Hurricanes/techprogram/paper_138319.htm.]

Cangialosi, J. P., S. S. Chen, W. Zhao, W. Wang, and J. Michalakas, 2006: Real-time high-resolution MM5 and WRF forecasts during RAINEX. Preprints, *27th Conf. on Hurricanes and Tropical Meteorology,* Monterey, CA, Amer. Meteor. Soc., 12A.4. [Available online at http://ams.confex.com/ams/pdfpapers/108876.pdf.]

Chen, S. S., W. Zhao, J. E. Tenerelli, R. H. Evans, and V. Halliwell, 2001: Impact of the AVHRR sea surface temperature on atmospheric forcing in the Japan/East Sea. *Geophys. Res. Lett.,* **28,** 4539–4542.

——, J. Knaff, and F. D. Marks, 2006: Effects of vertical wind shear and storm motion on tropical cyclone rainfall asymmetries deduced from TRMM. *Mon. Wea. Rev.,* **134,** 3190–3208.

——, J. F. Price, W. Zhao, M. A. Donelan, and E. J. Walsh, 2007: The CBLAST-Hurricane Program and the next-generation fully coupled atmosphere–wave–ocean models for hurricane research and prediction. *Bull. Amer. Meteor. Soc.,* **88,** 311–317.

Chen, Y., and M. K. Yau, 2001: Spiral bands in a simulated hurricane. Part I: Vortex Rossby wave verification. *J. Atmos. Sci.,* **58,** 2128–2145.

Dudhia, J., 1993: A nonhydrostatic version of the Penn State–NCAR Mesoscale Model. Validation tests and simulation of an Atlantic cyclone and cold front. *Mon. Wea. Rev.,* **121,** 1493–1513.

Garratt, J. R., 1992: *The Atmosphere Boundary Layer.* Cambridge University Press, 316 pp.

Grell, G., J. Dudhia, and D. R. Stauffer, 1994: A description of the fifth-generation Penn State/NCAR Mesoscale Model (MM5). NCAR Tech. Note NCAR/TN-398+STR, 138 pp.

Guinn, T. A., and W. H. Schubert, 1993: Hurricane spiral bands. *J. Atmos. Sci.,* **50,** 3380–3403.

Hence, D., and R. A. Houze, 2008: Kinematic structures of convective-scale elements in the rainbands of Hurricanes Katrina and Rita (2005). *J. Geophys. Res.,* **113,** D15108, doi:10.1029/2007JD009429.

Houze, R. A., 2010: Clouds of tropical cyclones. *Mon. Wea. Rev.,* **138,** 293–344.

——, and Coauthors, 2006: The Hurricane Rainband and Intensity Change Experiment (RAINEX): Observations and modeling of Hurricanes Katrina, Ophelia, and Rita (2005). *Bull. Amer. Meteor. Soc.,* **87,** 1503–1521.

——, S. S. Chen, B. Smull, W.-C. Lee, and M. Bell, 2007: Hurricane intensity and eyewall replacement. *Science,* **315,** 1235–1239.

Kain, J. S., and J. M. Fritsch, 1993: Convective parameterization for mesoscale models: The Kain–Fritsch scheme. *The Representation of Cumulus Convection in Numerical Models, Meteor. Monogr.,* No. 46, 165–170.

Kossin, J. P., and M. Sitkowski, 2009: An objective model for identifying secondary eyewall formation in hurricanes. *Mon. Wea. Rev.,* **137,** 876–892.

——, W. H. Schubert, and M. T. Montgomery, 2000: Unstable interactions between a hurricane's primary eyewall and a secondary ring of enhanced vorticity. *J. Atmos. Sci.,* **57,** 3893–3917.

Kuo, H.-C., L.-Y. Lin, C.-P. Chang, and R. T. Williams, 2004: The formation of concentric vorticity structures in typhoons. *J. Atmos. Sci.,* **61,** 2722–2734.

——, W. H. Schubert, C.-L. Tsai, and Y.-F. Kuo, 2008: Vortex interactions and barotropic aspects of concentric eyewall formation. *Mon. Wea. Rev.,* **136,** 5183–5198.

Ming, J., S. S. Chen, W. Zhao, and J. Michalakes, 2008: Distinct structure and intensity of Hurricanes Katrina and Ophelia (2005) in coupled WRF-HYCOM model. *Extended Abstracts, 28th Conf. on Hurricanes and Tropical Meteorology,* Orlando, FL, Amer. Meteor. Soc., 2A.3. [Available online at http://ams.confex.com/ams/28Hurricanes/techprogram/paper_138246.htm.]

Montgomery, M. T., and R. J. Kallenbach, 1997: A theory for vortex Rossby-waves and its application to spiral bands and intensity changes in hurricanes. *Quart. J. Roy. Meteor. Soc.,* **123,** 435–465.

Oda, M., T. Itano, G. Naito, M. Nakanishi, and K. Tomine, 2005: Destabilization of the symmetric vortex and formation of the elliptical eye of Typhoon Herb. *J. Atmos. Sci.,* **62,** 2965–2976.

Rogers, R., S. S. Chen, J. E. Tenerelli, and H. E. Willoughby, 2003: A numerical study of the impact of vertical shear on the distribution of rainfall in Hurricane Bonnie (1998). *Mon. Wea. Rev.,* **131,** 1577–1599.

Rozoff, C. M., W. H. Schubert, B. D. McNoldy, and J. P. Kossin, 2006: Rapid filamentation zones in intense tropical cyclones. *J. Atmos. Sci.,* **63,** 325–340.

Samsury, C. E., and E. J. Zipser, 1995: Secondary wind maxima in hurricanes: Airflow and relationship to rainbands. *Mon. Wea. Rev.,* **123,** 3502–3517.

Schubert, W. H., M. T. Montgomery, R. K. Taft, T. A. Guinn, S. R. Fulton, J. P. Kossin, and J. P. Edwards, 1999: Polygonal eyewalls, asymmetric eye contraction, and potential vorticity mixing in hurricanes. *J. Atmos. Sci.,* **56,** 1197–1223.

Tao, W. K., J. Simpson, C. H. Sui, B. Ferrier, S. Lang, J. Scala, M. D. Chou, and K. Pickering, 1993: Heating, moisture, and water budgets of tropical and midlatitude squall lines: Comparisons and sensitivity to longwave radiation. *J. Atmos. Sci.,* **50,** 673–690.

Tenerelli, J. E., and S. S. Chen, 2001: High-resolution simulation of Hurricane Floyd (1999) using MM5 with a vortex-following mesh refinement. Preprints, *14th Conf. on Numerical Weather Prediction,* Ft. Lauderdale, FL, Amer. Meteor. Soc., JP1.11. [Available online at http://ams.confex.com/ams/pdfpapers/23165.pdf.]

Terwey, W. D., and M. T. Montgomery, 2008: Secondary eyewall formation in two idealized, full-physics modeled hurricanes. *J. Geophys. Res.,* **113,** D12112, doi:10.1029/2007JD008897.

Wang, Y., 2002a: Vortex Rossby waves in a numerically simulated tropical cyclone. Part I: Overall structure, potential vorticity, and kinetic energy budgets. *J. Atmos. Sci.,* **59,** 1213–1238.

——, 2002b: Vortex Rossby waves in a numerically simulated tropical cyclone. Part II: The role in tropical cyclone structure and intensity changes. *J. Atmos. Sci.,* **59,** 1239–1262.

——, 2008: Rapid filamentation zone in a numerically simulated tropical cyclone. *J. Atmos. Sci.,* **65,** 1158–1181.

Willoughby, H. E., 1998: Tropical cyclone eye thermodynamics. *Mon. Wea. Rev.,* **126,** 3053–3067.

——, J. A. Clos, and M. G. Shoreibah, 1982: Concentric eye walls, secondary wind maxima, and the evolution of the hurricane vortex. *J. Atmos. Sci.,* **39,** 395–411.

Zhang, D., and R. A. Anthes, 1982: A high-resolution model of the planetary boundary layer—Sensitivity tests and comparisons with SESAME-79 data. *J. Appl. Meteor.,* **21,** 1594–1609.